Research Article Vol. 33, No. 25 / 15 Dec 2025 / Optics Express 52587
Optics EXPRESS

# Distributed measurement of gas pressure in the core of hollow-core optical fibres using nonlinear optics

MITCHELL GERRARD,* RADAN SLAVÍK, AND PETER HORAK

*Optoelectronics Research Centre, University of Southampton, Southampton SO17 1BJ, United Kingdom*
*mg6u19@soton.ac.uk

**Abstract:** We investigate theoretically and numerically the use of nonlinear optics to measure the spatial distribution of the gas density in the core of antiresonant hollow-core optical fibres. Short pump and signal laser pulses at different wavelengths and with controlled delay are launched into the fibre. Due to their different group velocity, they overlap within a certain region of the fibre where their nonlinear interaction create an idler pulse (via four-wave mixing) and/or the signal pulse experiences a nonlinear phase shift induced by the pump pulse via cross phase modulation. As the optical nonlinearity in these fibres is dominated by the gas content, a measurement of the idler power or signal phase shift at the fibre output thus provides information about the gas density (its pressure) at the pulse overlap position. We discuss the feasibility of the scheme and its dependence on fibre and pulse parameters. We conclude that such distributed gas measurements are possible within current experimental parameters and can potentially measure pressures far below current experimental techniques with high spatial resolution.



## 1. Introduction

Rapid progress in the development of antiresonant hollow-core optical fibres (AR-HCFs) in recent years has made them outperforming conventional solid-core silica fibres in many aspects. Today's low-loss AR-HCFs create antiresonant guiding with capillaries that surround the core [1]. Improvements via non-touching, separated capillaries [2] and nested capillary elements in antiresonant nodeless fibres (NANFs) [3] and double-nested antiresonant fibres (DNANF) [4] have led to record AR-HCFs [5] with losses below those of the best solid single-mode fibres [6]. Controlling the gas composition and density in the fibre core could unlock even lower attenuation levels [7] and reduce light absorption by the gas for long-distance communication [8].

Control of the gas density inside the hollow core of AR-HCFs is also crucial for many high-power and nonlinear optics applications. For instance, in high-power laser delivery systems [9] understanding the gas density is essential to managing ionisation thresholds and heat dissipation [10]. In data transmission, signal integrity and capacity depend on fibre core gas density and composition not only via the gas absorption but also via the refractive index and optical nonlinearity including Raman and Brillouin scattering [11]. On the other hand, large gas pressures can be used to optimise nonlinear supercontinuum generation [12,13] and the formation of optical solitons [14].

Reducing the gas pressure in the fibre core could also address other fundamental limitations in AR-HCFs, e.g., in reducing thermoconductive noise, which impacts the stability of guided modes [15], and backscattering, which can limit signal fidelity and coherence [16] impacting, for example, the use of orbital angular momentum states [17] for high-dimensional optical communication [18].

#580378 https://doi.org/10.1364/OE.580378
Journal © 2025 Received 29 Sep 2025; revised 21 Nov 2025; accepted 24 Nov 2025; published 4 Dec 2025

Optics EXPRESS

Given that fibre core gas pressure and composition is of such significant importance for the use of AR-HCFs, there is thus a need for methods to accurately measure the internal gas pressure. However, to date this remains a challenging task. While water ingress from the fibre end has been used [19] for average pressure measurements, the current state-of-the-art technique for distributed pressure measurements is optical time-domain reflectometry (OTDR) [20,21]. This offers insights into the overall loss and scattering properties but is limited to pressures above 0.15 atm. Another possible approach is stimulated Brillouin scattering [22,23] which shows gain down to 0.5 bar of nitrogen but faces challenges in achieving large linewidths at low pressure. Given these constraints, there is a clear need for alternative, more sensitive diagnostic methods.

Here we propose what we believe to be a novel approach to gas density measurements within AR-HCFs based on cross-phase modulation (XPM) and four-wave mixing (FWM). Optical nonlinearity in gas-filled fibres has been the subject of recent studies, e.g., the feasibility of FWM in short sections of capillary and photonic crystal HCFs at different pressures for nonlinear optical applications has been demonstrated [24–26]. Exploiting FWM for a distributed measurement of the variations of chromatic dispersion along optical fibres has also been suggested [27,28]. Our proposed method combines nonlinear optics in hollow-core fibres, which is dominated by the gas content of the core as less than 0.01% of power is propagating in the glass for modern AR-HCFs, with distributed sensing and offers what we believe to be a new route for in situ monitoring of gas pressure and can be integrated into real-time feedback systems for active gas control.

Our paper is structured as follows. In Section 2 we outline the XPM and FWM-based methods and introduce our numerical approach. In Section 3 we present the fibre design used throughout this study. Our main simulation results are shown in Section 4. Finally, we summarise our findings in Section 5.

## 2. Proposed method and numerical modelling approach

The method for distributed measurement of the gas pressure in the core of AR-HCFs is outlined in Fig. 1. Two laser pulses, a strong pump pulse and a weaker signal pulse, are launched into the fibre with a controlled time delay. Pump and signal are at different wavelengths and thus travel at different group velocities, such that they will overlap inside a certain region of the fiber where they interact via the optical Kerr nonlinearity. This leads to the creation of a weak idler pulse via FWM and also imposes a nonlinear phase shift on the signal via XPM. At the output of the fibre, the idler power or the signal phase can be measured to determine the strength of the nonlinear interaction in the region where the pulses overlapped. As discussed below, the nonlinearity in AR-HCF is dominated by the gas density in the fibre core, which itself depends on the local gas pressure. The output idler power or signal phase thus provide information on the local fibre core gas pressure. By repeating the experiment with different time delays between pump and signal at the launch, a spatially resolved gas pressure profile along the fibre length can be measured.

To investigate these two methods numerically, we solve the Nonlinear Schrödinger Equation (NLSE) [29], assuming that AR-HCFs are effectively single-mode [3] due to the high propagation loss of higher-order modes and that their hollow-core design renders them effectively polarisation-degenerate and minimally birefringent,

$$\frac{\partial A}{\partial z} + \frac{\alpha}{2}A - \sum_{k\geq 2} \frac{i^{k+1}}{k!}\beta_k \frac{\partial^k A}{\partial t^k} = i\gamma(p(z))\left(1 + i\frac{1}{\omega_p}\frac{\partial}{\partial t}\right)\left(A(z,t)|A(z,t)|^2\right) \tag{1}$$

where $A(z,t)$ is the amplitude of the propagating field at time $t$ and position $z$ along the fibre and $\beta_k$ is the $k$-th derivative of the propagation constant $\beta$ with respect to angular frequency taken at the frequency of the pump $\omega_p$. Note that we neglect the Raman nonlinearity here, as for the power levels and 1 ps pulses used below, its effect is minor in air, where the dominant nitrogen line has a >75 ps delay time at pressures up to 1 atm; for other gases and higher pressures Raman scattering

Optics EXPRESS

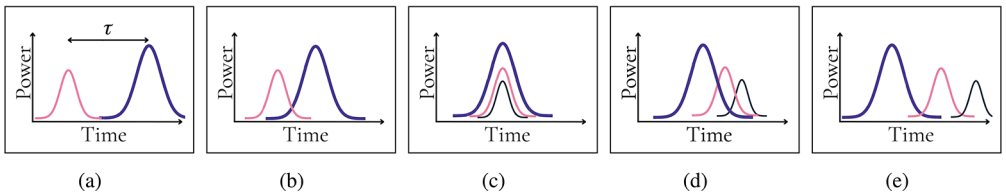


**Fig. 1.** (a) A high-power pump (purple) and a low-power signal (pink) at different wavelengths are launched into the fibre with a time delay $\tau$. (b) As the pulses propagate through the fibre with different group velocities, they begin to overlap. (c) The pulses fully overlap; optical nonlinearity results in an XPM-induced phase shift of the signal and the generation of an idler pulse via FWM. (d) Group-velocity dispersion causes the pulses to separate again until (e) they are fully separated at the fibre output where the nonlinear response is measured.

can be included in the NLSE [30]. Equation (1) holds under the simplifying assumption of a single linear polarisation of the laser pulses throughout the propagation. Depending on the fibre properties this may not be achievable in an experiment, in which case polarisation averaging or numerical treatment via a Manakov equation [31] may be required. The fibre propagation loss is given by $\alpha$ and the nonlinear coefficient by

$$\gamma(p) = \frac{2\pi(n_2^{air}(p)\int_{air}|E|^4dxdy + n_2^{glass}\int_g|E|^4dxdy)}{\lambda_p(\int|E|^2dxdy)^2} \tag{2}$$

where $\lambda_p$ is the pump wavelength, $n_2^{air}(p)$ is the nonlinear refractive index of the air at pressure $p$ in the fibre ($n_2^{air}(1\text{ atm}) = 5.57\times10^{-23}$ m$^2$/W [32–34]) and $n_2^{glass} = 2.2\times10^{-20}$ m$^2$/W is the nonlinear refractive index of silica [35]. $E$ is the electric field of the fundamental mode of the fibre, and the integrals are over the air, glass, and full cross section of the fibre, respectively. Equation (1) is solved using a split-step Fourier technique with automated step size control and a Runge-Kutta 5th-order method for the nonlinear propagation steps in the Python programming language.

At the end of the simulation, i.e., at the fibre output, the amplitude $A$ is spectrally filtered to separate the pump, signal, and idler amplitudes $A_p(t)$, $A_s(t)$, and $A_i(t)$. The relevant quantities for our pressure measurement methods are the integrated idler output power,

$$P_i = \int |A_i(t)|^2 dt, \tag{3}$$

and the phase of the output signal pulse which we define as an intensity-weighted average over the signal amplitude $A_s(t)$

$$\phi_s = \frac{\int arg(A_s(t))|A_s(t)|^2dt}{\int|A_s(t)|^2dt}. \tag{4}$$

The signal phase $\phi_s$ contains contributions from linear propagation, self-phase modulation etc. in addition to the desired XPM phase induced by the pump. We thus extract the pure XPM phase shift as

$$\phi_{s,XPM} = \phi_s - \phi_{s,0} \tag{5}$$

where $\phi_{s,0}$ is the reference signal phase obtained from a simulation without a pump pulse, thereby removing any phase accumulated from unrelated mechanisms. Note that this equation holds for parameters far from the phase-matching condition, where FWM-induced changes to the signal are negligible. From Eq. (1) it is clear that $\phi_{s,XPM}$ will depend linearly on $\gamma(p(z_0))$ and $P_i$ will be

Optics EXPRESS

proportional to the square $\gamma(p(z_0))^2$ where $p(z_0)$ is the pressure in the fibre core at the position $z_0$ where pump and signal pulses overlap, given by

$$z_0 = \frac{\tau}{|v_{g,p}^{-1} - v_{g,s}^{-1}|} \tag{6}$$

where $v_{g,p}$ and $v_{g,s}$ are the group velocities of pump and signal and $\tau$ is the difference in launch time between them, assuming the slower wave is released first. Thus, if $P_i$ or $\phi_{s,XPM}$ are measured, the pressure at position $z_0$ can be obtained by comparison with numerical simulations. In situations where a reference experiment (or an equivalent simulation) can be performed with the fibre at a constant internal pressure $p_{ref}$, the pressure $p(z_0)$ can be directly obtained by the XPM-based and FWM-based method, respectively, as

$$p(z_0) = \frac{\phi_{s,XPM}}{\phi_{s,XPM}(p_{ref})} \quad \text{or} \quad p(z_0) = \sqrt{\frac{P_i}{P_i(p_{ref})}}. \tag{7}$$

Note that Eq. (7) applies in the limit where the gas nonlinearity dominates over the contribution from the glass, see Sec. 3.

To aid our understanding of these processes, it is instructive to consider the quasi-continuous wave (CW) case. In this limit, the XPM phase is

$$\phi_{s,XPM} = 4\gamma P_p L_w \tag{8}$$

where $L_w$ is the walk-off length, i.e., the length of fibre where pump and signal pulses of duration $T_0$ overlap,

$$L_w = \frac{T_0}{|v_{g,p}^{-1} - v_{g,s}^{-1}|}. \tag{9}$$

Degenerate FWM creates an idler at $\omega_i = 2\omega_p - \omega_s$ where $\omega_{p,s,i}$ are the angular frequencies of pump, signal, and idler, respectively. In the small-idler, no pump depletion limit, the integrated idler power is [36]

$$P_i = T_0 \left( \frac{\gamma |A_p|^2 |A_s|}{\Delta\beta} \right)^2 \left| e^{i2\Delta\beta L_w} - 1 \right|^2 \tag{10}$$

which in addition to $L_w$ crucially depends on the phase mismatch

$$\Delta\beta = 2\beta_p - \beta_s - \beta_i + 2\gamma P_p \tag{11}$$

where $\beta_{p,s,i}$ are the various propagation constants and $P_p$ is the pump power. It is clear from Eqs. (8), (10) that by reducing the walk-off length, i.e., reducing the length over which the pump and signal overlap, we can get better resolution on our pressure measurement, but at the cost of weaker idler power and signal phase shift. In addition, for the FWM-based method we need to operate at wavelengths leading to small phase mismatch in order to generate an observable idler power, as will be discussed in more detail in the following section.

## 3. Hollow-core fibre parameters

In this study we assume a perfectly symmetric, idealised 7-tube antiresonant hollow-core fibre (inset of Fig. 2(a)) with a core radius of 20.5 $\mu$m, capillary radius of 5.64 $\mu$m, and capillary wall thickness of 446 nm operating in the fundamental window, similar to the fibre used by Kelly et al. [37]. Note that in the calculations in this paper we ignore propagation losses, although it would be straightforward to include them in the analysis, in order to focus predominantly on the nonlinear effects. For practical lengths of fibre, the AR-HCF of Fig. 2 would have too high propagation losses and lower loss NANFs or DNANFs would be used.

Optics EXPRESS

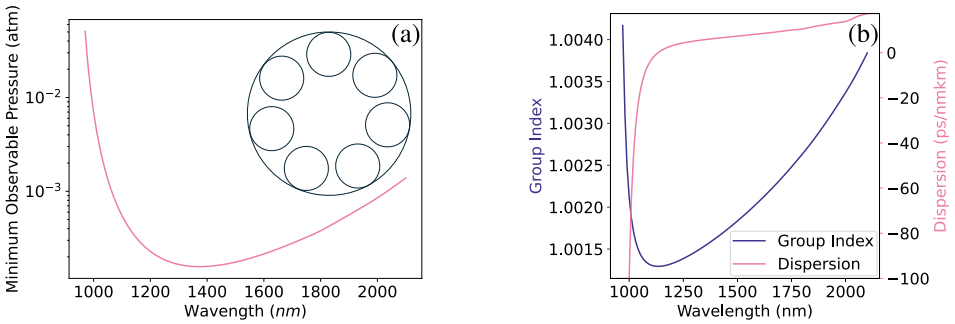


**Fig. 2.** (a) Minimum observable air pressure given by Eq. (12) for the sample fibre structure (inset) used in this study. (b) Group index and group velocity dispersion of the fundamental mode of the fibre.

We simulate the fibre properties using a mode analysis based on the finite-element method (COMSOL Multiphysics) within the Electromagnetic Waves, Frequency Domain module, incorporating the full anti-resonant fibre geometry and the material refractive indices. The simulations calculate the fundamental mode, its propagation constant, and its effective mode area over the wavelength range of interest. These results are then used in the NLSE, Eq. (1), implemented in Python.

We determine the minimum gas pressure measurable by our method, i.e., the pressure at which the gas contribution to the optical nonlinearity equals that of the glass in Eq. (2), as

$$\frac{p_{min}(\lambda)}{1\ \text{atm}} = \frac{n_2^{glass} \int_g |E(\lambda)|^4 dxdy}{n_2^{air}(1\ \text{atm}) \int_{air} |E(\lambda)|^4 dxdy}, \tag{12}$$

shown in Fig. 2(a). We find that in the wavelength region of 1060-1600 nm the minimum observable pressure is $1 - 5 \times 10^{-4}$ atm, thus allowing for pressure measurements over 3.5 orders of magnitude below atmospheric pressure. For lower gas pressures, the nonlinear effect of the glass will dominate. Note, however, that this could still be taken into account in the analysis as long as the signal-to-noise ratio of the measured values of $P_i$, $\phi_{s,XPM}$ is sufficiently high. Two orders of magnitude lower gas pressures can still be observed in improved fibre designs such as NANFs [3] and DNANFs [4] that have better confinement in the core of the fibre.

The group index and the group velocity dispersion of the fundamental mode are shown in Fig. 2(b). The fibre exhibits a fundamental transmission window starting near 892 nm; significant dispersion is observed in the vicinity of this resonance. The zero dispersion wavelength (ZDW) is at 1134 nm. The group index has a minimum at the ZDW, leading to the fastest pulses at that wavelength.

Further analysis of the dispersion properties of this fibre is shown in Fig. 3. In (a) we show the phase mismatch $\Delta\beta$, Eq. (11), versus pump and signal wavelength, where the idler wavelength is chosen according to the energy conservation condition ($\omega_i = 2\omega_p - \omega_s$). Phase matching, leading to strong idler generation, is expected when pump, signal, and idler are close together (diagonal line in the figure) or when operating near the ZDW (near-vertical feature near 1134 nm). Away from these two regions, the coherence length $1/\Delta\beta$ quickly reduces to the sub-metre regime.

The walk-off length $L_w$, Eq. (9), is shown in Fig. 3(b). We see two regions of large walk-off lengths, one where the pump is close to the signal and the second around the minimum of the group index of Fig. 2(b) where signal and pump wavelengths can be chosen with the same group index. As mentioned before, these parameter regimes will lead to stronger nonlinear effects, but simultaneously to poor spatial resolution of the pressure measurements and a compromise must be found for the purposes of our study. For the FWM-based approach, the phase mismatch

Optics EXPRESS

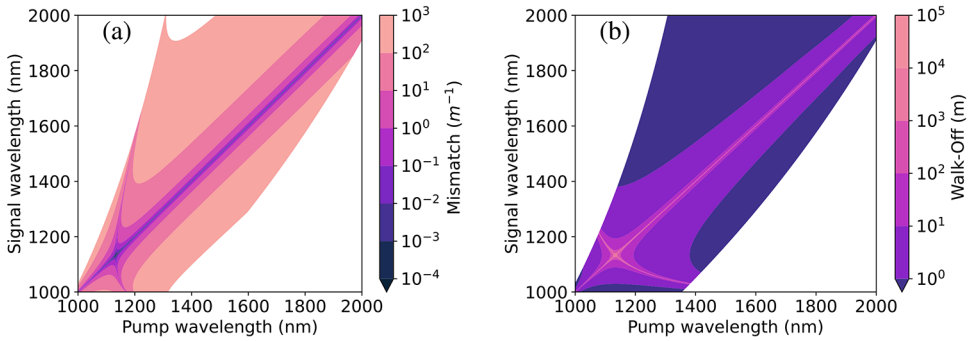


**Fig. 3.** (a) Phase mismatch ($\Delta\beta$) vs signal and pump wavelength for the fibre of Fig. 2. (b) Corresponding walk-off length $L_w$ vs pump and signal wavelength for 1 ps pulses.

curve implies the use of a pump in the anomalous dispersion regime. The signal wavelength could then be chosen in the normal-dispersion regime to achieve better resolution due to a shorter walk-off length. However, in this regime the signal will experience stronger dispersive pulse broadening. To minimise the effect of broadening, we will in the following use a signal in the anomalous dispersion regime. For the FWM-based approach this then puts the idler into the normal dispersion regime; however our method is less sensitive to idler pulse distortion than to signal distortions.

## 4. Simulations of nonlinear optics pressure measurements

### *4.1. XPM-based approach*

We first investigate the XPM method of distributed AR-HCF pressure measurement, which is based on the nonlinear XPM phase shift of the signal pulse. As discussed in Sec. 2, this has the advantage over the FWM-based method of not requiring phase matching, thus giving us more flexibility in selecting our pump and signal wavelengths. In particular, we can use the group index shown in Fig. 2 to choose wavelengths according to laser availability and difference in group velocity, where a larger difference in the group velocity yields a better spatial resolution. We pick two wavelength ranges of interest, one around 1550 nm in the telecommunications C band and one near the ZDW of the fibre. Unless stated otherwise, the delay in pump and signal pulses at the fibre input is chosen to be 2 ps, yielding overlapping pulses at positions 1.2 - 11.6 m within a 100 m long fibre.

Figure 4 shows the XPM phase shift $\phi_{s,XPM}$, Eq. (8), of the signal for a range of pulse parameters for our sample fibre. In Fig. 4(a) we see that for a spatial resolution of around 3-8 m with the most powerful pump (100 kW peak power of a 1 ps pulse) we obtain a phase shift of order 1 rad, which e.g. Mach–Zehnder interferometers can easily measure. We also observe that the phase scales linearly with the pump power and linearly with the pulse walk-off length, as expected. Figure 4(b) shows the same trends in the wavelength region near the ZDW. Comparing the two figures, we note that the phase shifts are approximately the same for the same spatial resolution and pump powers, as expected from the analytic approximation of Eq. (8). For example, at a resolution of 5 m and for 100 kW peak powers, the nonlinear phase shifts are 0.69 rad for the 1550 nm pump and 0.67 rad for the 1150 nm pump, with the small differences attributed to the slight difference in mode area calculated by Comsol Multiphysics to be $1.95 \times 10^{-10}$ m$^2$ at 1150 nm and $1.84 \times 10^{-10}$ m$^2$ at 1550 nm.

In Fig. 5, the phase shift is observed to scale linearly with pressure, as expected from theory. The differences in gradient arise from variations in mode area and walk-off length at different

Optics EXPRESS

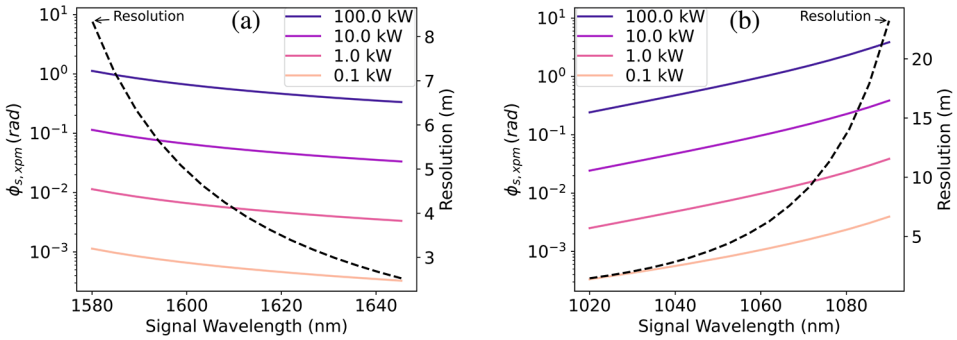


**Fig. 4.** Nonlinear XPM phase shift $\phi_{s,XPM}$ of the signal vs signal wavelength and for pump peak powers 0.1-100 kW with pump wavelengths of (a) 1550 nm and (b) 1150 nm. Pulse length is 1 ps, signal peak power 1W and pressure 1 atm. The resulting spatial resolution, given by $2L_w$, is also shown.

wavelengths, demonstrating that longer pulse interactions lead to stronger XPM phase shifts. This confirms that the expected model can be reliably used to track pressure in AR-HCFs

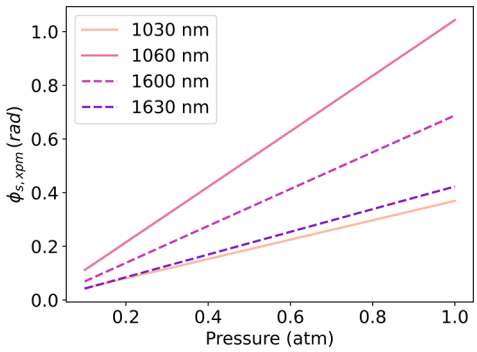


**Fig. 5.** XPM phase shift vs pressure for pump $\lambda_p = 1550$ nm and signals $\lambda_s = 1600$ nm and 1630 nm (dashed lines) with resolution of 4.95 m and 3.04 m, respectively, and for pump $\lambda_p = 1150$ nm, and signals $\lambda_s = 1030$ nm and 1060 nm (solid lines) with resolution of 2.04 m and 5.82 m, respectively.

To test the distributed pressure measurement using the XPM-based scheme we define two sample pressure distributions $p_{1,2}(z)$ (in units of 1 atm) as

$$p_1(z) = \sqrt{1 - \frac{z}{L}(1 - 0.001^2)}, \quad p_2(z) = \begin{cases} 0.6 \text{ atm}, & 0 \le z < \frac{L}{2} \\ 0.2 \text{ atm}, & \frac{L}{2} \le z \le L \end{cases} \tag{13}$$

and use these in the NLSE to simulate the pump and signal propagation through a 100 m long fibre. In Fig. 6(a) we compare the analytical input $p_1(z)$ and our reconstructed pressure profile using Eq. (7) for a pump wavelength in the telecommunication C band and find excellent agreement. This pressure profile is only slowly varying and does not require high spatial resolution for precise distributed measurements. We thus investigate the reconstruction of the step-profile $p_2(z)$ in Fig. 6(b). Here we can clearly see the limitations of the spatial resolution given by the walk-off length between pump and signal pulses. Increasing the wavelength difference between pump and signal by moving the signal wavelength from 1600 nm to 1630 nm shows the expected improvement in spatial resolution from 4.55 m to 2.8 m, see Fig. 4, given by the larger group

Optics EXPRESS

velocity difference and thus shorter walk-off length. In these simulations we used 100 time delays between the launched pump and signal pulses, i.e., we ran 100 simulations of the NLSE. Note, however, that the spatial resolution is determined by the walk-off length and not by the number of pulses. Similar results are obtained if pump and signal wavelengths are chosen close to the ZDW of the fibre, Figs. 6(c,d), demonstrating that this method works well at any choice of wavelengths.

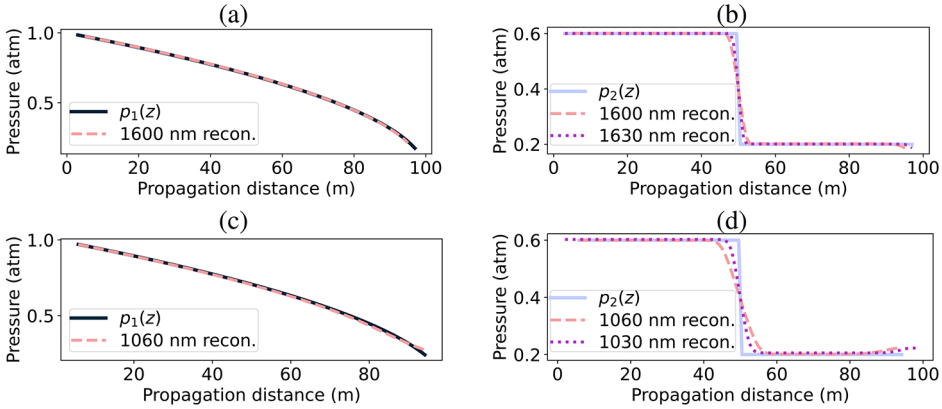


**Fig. 6.** Distributed pressure measurements using the XPM-based method. Two sample pressure profiles $p_1(z)$ (a,c) and $p_2(z)$ (b,d) are used in the NLSE simulations and then reconstructed from the signal output phase for 100 kW pump, 1 W signal peak powers at different wavelengths: (a) $\lambda_p$ = 1550 nm, $\lambda_s$ = 1600 nm, (b) $\lambda_p$ = 1550 nm, $\lambda_s$ = 1600 nm and 1630 nm, (c) $\lambda_p$ = 1150 nm, $\lambda_s$ = 1060 nm, (d) $\lambda_p$ = 1150 nm, $\lambda_s$ = 1030 nm and 1060 nm.

### 4.2. *FWM-based approach*

We now investigate the FWM-based pressure measurement approach. In Fig. 7(a), we explore the effect of the pump peak power on the idler output power as we sweep across the pump wavelength in the anomalous dispersion region close to the ZDW. For each pump wavelength the signal and idler wavelengths are chosen to satisfy the phase matching condition (Fig. 3(a)). The delay between pump and signal pulses is again chosen to be 2 ps, yielding overlapping pulses at positions 0.66 - 8.77 m in a 100 m long fibre. As the wavelength moves further from the ZDW, the resolution improves caused by shorter walk-off lengths but idler output power reduces. When both the pump and signal powers are reduced by an order of magnitude, we lose three orders of magnitude from the idler power output, in line with Eq. (10). Thus, maximising the available pump power is imperative for this scheme to work.

In Fig. 7(b), we show the idler power as a function of pump wavelength and for the fibre filled uniformly with different gas pressures. As discussed in Section 2, the idler drops quadratically with the pressure reduction.

Next, we test the distributed pressure measurement using the FWM-based scheme to demonstrate the system's resolution. The pressure profiles defined in Eq. (13) are used in the NLSE to simulate pump, signal, and idler propagation through a 100 m long fibre, using 100 simulations with different launch delays between pump and signal pulses to cover the fibre length. From the output idler power we then reconstruct the pressure profile, as discussed previously.

The reconstruction of profile $p_1(z)$ is shown in Fig. 8(a) for a pump wavelength of 1140 nm near the ZDW for two different pump powers of 2.5 kW and 10 kW with corresponding signal powers of 1.25 kW and 5 kW, respectively. For 2.5 kW pump peak power, this FWM-based method produces a highly accurate distributed measurement of the pressure profile. Using too high powers, such as 10 kW, on the other hand, deteriorates the accuracy of the reconstructed

Optics EXPRESS

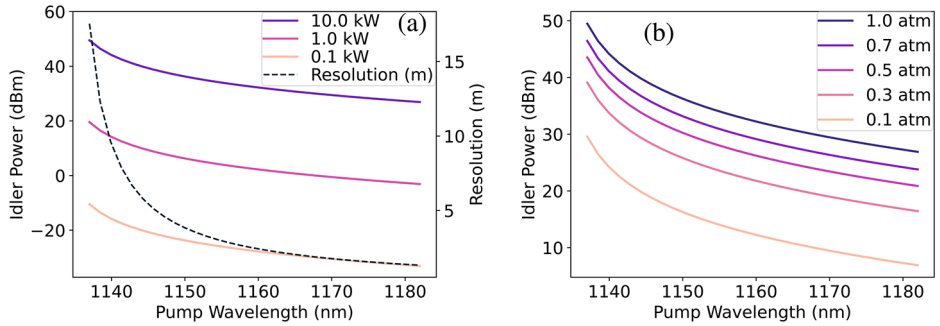


**Fig. 7.** Idler power vs pump wavelengths near the fibre ZDW. (a) Idler power for pump peak powers of 100 W to 10 kW. Pulse length is 1 ps, pressure 1 atm, and signal power is one half of the pump power. Also shown is the spatial resolution of the FWM-based pressure measurement, given by $2L_w$, Eq. (9). (b) Idler power for pressures of 0.1-1 atm with pump peak power of 10 kW and signal peak power of 5 kW.

pressure profile; this is due to self-phase modulation induced broadening of the pump pulses at 1 atm leading to greater than expected idler output power. The limiting pump power can be estimated from the SPM phase shift, given by $\gamma PL$, which should by $\ll \pi$ but for 10 kW here is 1.5 rad. Figure 8(b) shows the (numerical) distributed measurement of the step pressure profile $p_2(z)$ at the lower peak pump power of 2.5 kW. For a pump wavelength of 1140 nm the spatial resolution is limited to 9.55 m (see Fig. 7) which improves to a resolution of 1.2 m for a pump wavelength of 1160 nm with corresponding wider signal and idler separation.

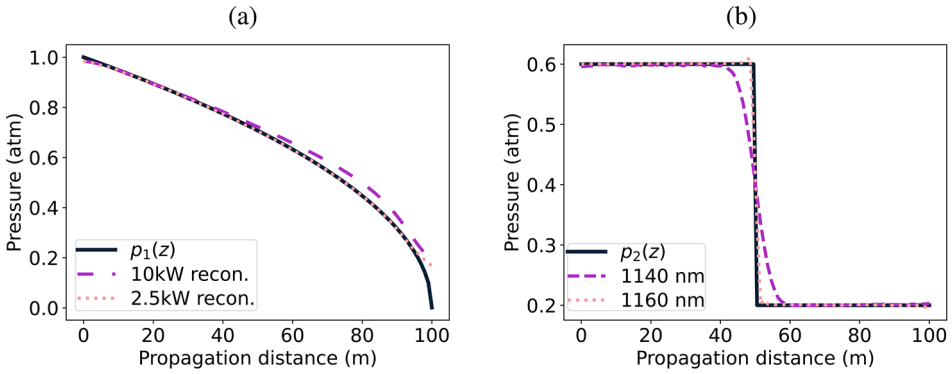


**Fig. 8.** Distributed pressure measurements using the FWM-based method. (a) The sample pressure profile $p_1(z)$, Eq. (13), is used in the NLSE simulations and then reconstructed from the idler output powers for 2.5 kW pump/1.25 kW signal and 10 kW pump/5 kW signal for wavelengths $\lambda_p = 1140$ nm, $\lambda_s = 1065$ nm, $\lambda_i = 1226$ nm. (b) Reconstruction of pressure profile $p_2(z)$ at 2.5 kW pump/1.25 kW signal power and wavelengths as in (a) and with wavelengths $\lambda_p = 1160$ nm, $\lambda_s = 1014$ nm, $\lambda_i = 1355$ nm.

In Fig. 8 we chose pump wavelengths relatively close to the ZDW. As already discussed in Fig. 3, phase matching can also be approximately achieved far away from the ZDW if pump, signal, and idler are close together in wavelength. This region includes the telecommunication C band around 1550 nm where most AR-HCFs are designed to have minimum loss.

We analyse the coherence length, $L_{\text{coh}} = 2\pi/\Delta\beta$, and walk-off length near 1550 nm in Fig. 9. To achieve effective FWM, Eq. (10) implies that the coherence length exceeds the walk-off length, otherwise power is periodically transferred back from the idler into the pump. As shown in the

Optics EXPRESS

figure, this limits the available bandwith of signal wavelengths to around 2 nm for 1 ps pulses and 33 nm for 0.1 ps pulses. On the other hand, the transform limited bandwidth of 1 ps pulses is 3.5 nm and for 0.1 ps pulses it is 35 nm. We therefore find that efficient FWM can only be achieved with pulses that spectrally overlap. It is thus not possible to separate the idler pulse from the pump at the fibre output and our FWM-based distributed pressure measurement technique cannot be applied in this pump wavelength regime.

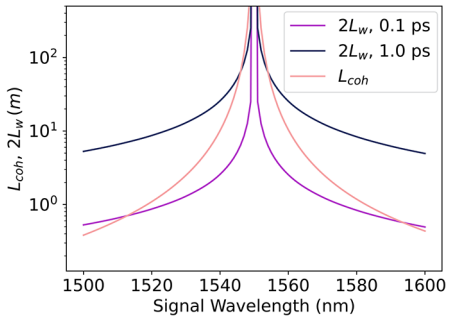


**Fig. 9.** Coherence length $L_{\mathrm{coh}}$ and the overlap distance $2L_w$ of signal and pump pulses for a pump at 1550 nm vs signal wavelength for pulse widths of 0.1 ps and 1 ps for the chosen AR-HCF.

### 4.3. *Impact of fibre non-uniformity*

Real fabricated AR-HCFs are not completely uniform, but the geometry can vary significantly along the fibre length [38], which can have a large impact on the fibre dispersion properties. We thus examine in this section how changes in fibre geometry affect the FWM idler generation and the XPM signal phase shift as the essential quantities of interest for our distributed pressure measurements. Specifically, we investigate the effect when changing the thickness of the capillaries in the AR-HCF from 446 nm to 446 ± 10 nm (approximately 4% change). Note that a fluctuation in capillary wall thickness is accompanied by a change in capillary diameter such that the total cross section area of glass (i.e., its mass) is conserved.

Figure 10 shows the change in chromatic dispersion properties of the AR-HCF with varying capillary thickness. Figure 10(a) shows a significant shift of the zero dispersion wavelength by about 25 nm, from 1133.7 nm at 446 nm capillary thickness to 1109.2 nm at 436 nm and 1158.1 nm at 456 nm, which will significantly affect the phase matching condition of FWM. In this figure and the group index shown in Fig. 10(b) we see that changes in the capillary thickness mostly affect the wavelength region near the high-loss resonance and the ZDW, while for wavelengths far above the ZDW the group velocity dispersion differences are smaller and thus, for example, the distance at which signal and pump pulses overlap and the walk-off length will be less affected.

In Fig. 11(a) we see that the shift in the ZDW for fibres with even small changes of the capillary thickness causes a significant change in the achievable FWM idler power at given pump wavelength. Note that for the curves in this figure we assume that the signal/idler wavelength pair is chosen to fulfill phase matching. For the FWM-based pressure measurement in a fibre whose geometry varies along its length, this means that to maintain significant idler output power both the pump and the signal wavelength must be optimised depending on the position $z_0$, Eq. (6), where pump and signal overlap, making a potential experiment and data analysis much more complex, possibly requiring a separate measurement of the position dependent ZDW [27]. For the XPM-based method, on the other hand, the XPM induced nonlinear phase shift is only changing by less than 2%, as shown in Fig. 11(b) due to the relatively small changes in group delay in the chosen wavelength region (Fig. 10) and a similar small change in the

Optics EXPRESS

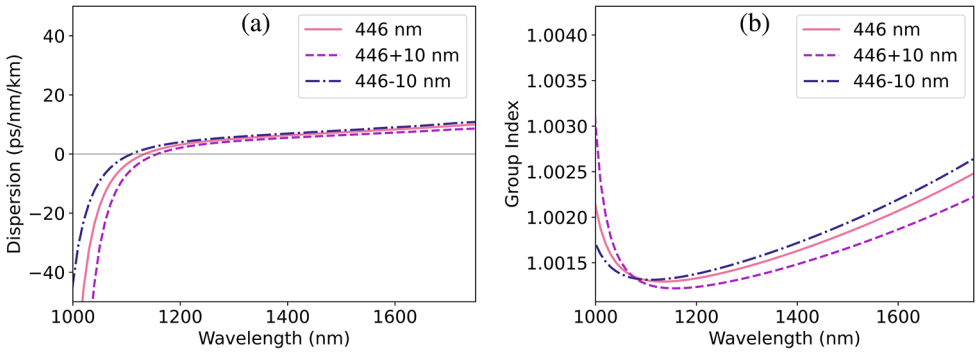


**Fig. 10.** Variation of AR-HCF properties with capillary thickness varied by 446 ± 10 nm for the fibre discussed in Sec. 3. (a) Dispersion parameter $D$ vs wavelength. (b) Group index vs wavelength.

nonlinearity $\gamma$ because of a varying mode area, which implies that even a relatively large fibre inhomogeneity would only introduce a 2% error in the pressure measurement. This demonstrates that the proposed XPM-based pressure measurement approach is much more robust against fibre geometry fluctuations than the FWM-based approach since XPM does not depend on fulfilling a stringent phase matching condition.

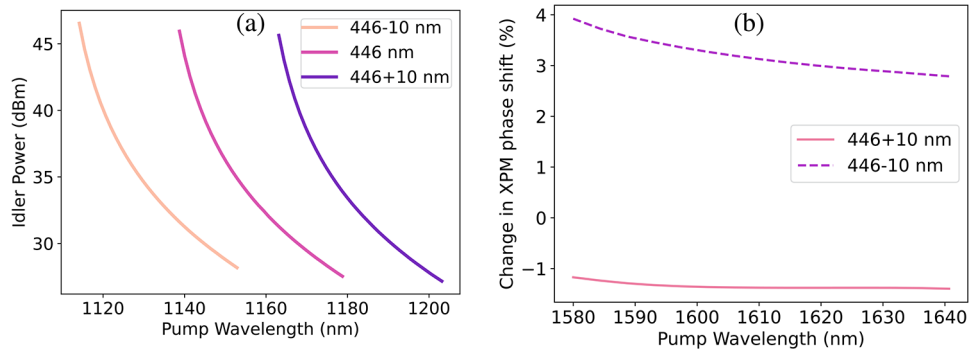


**Fig. 11.** (a) Idler output power for the AR-HCF with modified capillary thickness (given in the legend) vs pump wavelength near the ZDW. In each case, signal and idler are chosen to fulfill the phase matching condition. Peak pump power is 10 kW, peak signal power 5 kW. (b) Change of XPM signal phase shift relative to the results of Fig. 5(a) vs pump wavelength for peak pump power 100 kW, signal peak power 1 W. All simulations at 1 atm pressure for 1 ps pulse lengths.

## 5. Conclusions

We have proposed and numerically investigated two approaches to exploit nonlinear optical effects for distributed measurements of the gas pressure in the core of hollow-core optical fibres, one approach based on four-wave mixing, the other on cross phase modulation.

We have demonstrated that for realistic experimental parameters these methods offer a spatial resolution comparable to traditional OTDR measurements, reported as 5 m [20]. However, OTDR back-reflection signals are directly proportional to gas density and can fall within 10 dB of the detection noise floor [39,40], posing a significant constraint on the lowest measurable gas pressure. In contrast, our nonlinear techniques rely on spectrally separating the powers of the

Optics EXPRESS

pump, signal, and idler at the output and/or on measuring a signal phase, which could potentially achieve a substantially lower pressure detection limit. We estimate a detection limit of order $10^{-3}$ atm determined by the residual nonlinearity of the fraction of light propagating inside the glass, but note that highly sensitive photodectectors and/or stable interferometric or heterodyne detection may be required to achieve this limit.

The FWM-based method can work efficiently for laser wavelengths near the zero-dispersion wavelength of the fibre, though this may require a signal or idler wavelength closer to the edge of the fibre transmission window and thus at increased losses. It also relies on phase matching, which makes this method susceptible to fluctuations of the geometry along the fibre length. The XPM-based method, on the other hand, requires the measurement of the signal phase at the output and thus more complicated experimental setups, but works effectively at any wavelength and is much more robust against fibre fluctuations.

Finally, we note that the FWM idler power scales with the square of the pump laser power and with the square of the gas pressure, making this method more beneficial if high laser powers are available. In contrast, the XPM phase shift scales linearly with both laser power and gas pressure and may therefore be more suitable at lower gas pressures. The choice of the optimum distributed measurement method will thus depend on the operating parameters, such as available laser wavelengths, laser power, and confinement of the fibre.

**Funding.** UK Engineering and Physical Sciences Research Council (EP/W037440/1).

**Acknowledgments.** We acknowledge discussions with Seyed Mohammad Abokhamis Mousavi at the initial stages of the project.

**Disclosures.** The authors declare no conflicts of interest.

**Data availability.** Data underlying the results presented in this paper are available at [41] .

## References

1. A. D. Pryamikov, A. S. Biriukov, A. F. Kosolapov, *et al.*, "Demonstration of a waveguide regime for a silica hollow-core microstructured optical fiber with a negative curvature of the core boundary in the spectral region > 35 μm," Opt. Express **19**(2), 1441–1448 (2011).
2. A. N. Kolyadin, A. F. Kosolapov, A. D. Pryamikov, *et al.*, "Light transmission in negative curvature hollow core fiber in extremely high material loss region," Opt. Express **21**(8), 9514–9519 (2013).
3. F. Poletti, "Nested antiresonant nodeless hollow core fiber," Opt. Express **22**(20), 23807–23828 (2014).
4. G. T. Jasion, H. Sakr, J. R. Hayes, *et al.*, "0.174 dB/km Hollow Core Double Nested Antiresonant Nodeless Fiber (DNANF)," in *Optical Fiber Communication Conference (OFC) 2022*, (Optica Publishing Group, San Diego, California, 2022). Paper Th4C.7.
5. Y. Chen, M. Petrovich, E. N. Fokoua, *et al.*, "Hollow Core DNANF Optical Fiber with <0.11 dB/km Loss," in *Optical Fiber Communication Conference (OFC) 2024*, (Optica Publishing Group, San Diego California, 2024). Paper Th4A.8.
6. Y. Tamura, H. Sakuma, K. Morita, *et al.*, "The First 0.14-dB/km Loss Optical Fiber and its Impact on Submarine Transmission," J. Lightwave Technol. **36**(1), 44–49 (2018).
7. E. Numkam Fokoua, S. Abokhamis Mousavi, G. T. Jasion, *et al.*, "Loss in hollow-core optical fibers: mechanisms, scaling rules, and limits," Adv. Opt. Photonics **15**(1), 1–85 (2023).
8. D. Ge, M. Zuo, D. Wang, *et al.*, "Optical Transmission Based on Antiresonant Hollow-Core Fibers," in *2025 30th OptoElectronics and Communications Conference (OECC) and 2025 International Conference on Photonics in Switching and Computing (PSC)*, (IEEE, Sapporo, Japan, 2025). Paper MC3-1.
9. A. Lekosiotis, F. Belli, C. Brahms, *et al.*, "On-target delivery of intense ultrafast laser pulses through hollow-core anti-resonant fibers," Opt. Express **31**(19), 30227–30238 (2023).
10. A. V. Newkirk, J. M. Mercado, E. A. Lopez, *et al.*, "Anti-Resonant Hollow Core Fiber for High Power Laser Delivery," in *2021 IEEE Research and Applications of Photonics in Defense Conference (RAPID)*, (IEEE, Miramar Beach, FL, USA, 2021). Paper WC3.
11. X. Zhang, Z. Feng, D. Marpaung, *et al.*, "Low-loss microwave photonics links using hollow core fibres," Light: Sci. Appl. **11**(1), 213 (2022).
12. B. Plosz, A. Lekosiotis, M. Sabbah, *et al.*, "Supercontinuum generation in a methane-filled hollow-core antiresonant fiber," Opt. Lett. **50**(4), 1285–1288 (2025).
13. T. Sylvestre, E. Genier, A. N. Ghosh, *et al.*, "Recent advances in supercontinuum generation in specialty optical fibers [Invited]," J. Opt. Soc. Am. B **38**(12), F90–F103 (2021).
14. J. C. Travers, "Optical solitons in hollow-core fibres," Opt. Commun. **555**, 130191 (2024).

Optics EXPRESS


15. V. Michaud-Belleau, E. R. Numkam Fokoua, P. Horak, *et al.*, "Fundamental thermal noise in antiresonant hollow-core fibers," Phys. Rev. A **106**(2), 023501 (2022).
16. V. Michaud-Belleau, E. Numkam Fokoua, T. D. Bradley, *et al.*, "Backscattering in antiresonant hollow-core fibers: over 40 dB lower than in standard optical fibers," Optica **8**(2), 216–219 (2021).
17. D. Cozzolino, D. Bacco, B. Da Lio, *et al.*, "Orbital Angular Momentum States Enabling Fiber-based High-dimensional Quantum Communication," Phys. Rev. Appl. **11**(6), 064058 (2019).
18. A. Stefani, S. C. Fleming, and B. T. Kuhlmey, "Terahertz orbital angular momentum modes with flexible twisted hollow core antiresonant fiber," APL Photonics **3**(5), 051708 (2018).
19. S. Rikimi, Y. Chen, T. W. Kelly, *et al.*, "Internal Gas Composition and Pressure in As-drawn Hollow Core Optical Fibers," J. Lightwave Technol. **40**(14), 4776–4785 (2022).
20. R. Slavík, E. R. Numkam Fokoua, T. D. Bradley, *et al.*, "Optical time domain backscattering of antiresonant hollow core fibers," Opt. Express **30**(17), 31310–31321 (2022).
21. X. Wei, B. Shi, D. J. Richardson, *et al.*, "Distributed Characterization of Low-loss Hollow Core Fibers using EDFA-assisted Low-cost OTDR instrument," in *2023 Optical Fiber Communications Conference and Exhibition (OFC)*, (IEEE, San Diego, CA, USA, 2023). Paper W1C.4.
22. Y. Yang, M. A. Soto, and L. Thévenaz, "Absolute temperature sensing in the 67-350K range using Brillouin scattering in gases," Proc. SPIE **13639**, 136390S (2025).
23. L. Thévenaz, "Distributed optical fiber sensors: what is known and what is to come," Front. Sens. **6**, 1546392 (2025).
24. H. Zhang, L.-S. Sun, J. Hirschman, *et al.*, "Optimizing spectral phase transfer in four-wave mixing with gas-filled capillaries," Opt. Express **32**(25), 44397–44412 (2024).
25. F. Belli, A. Abdolvand, J. C. Travers, *et al.*, "Highly efficient deep UV generation by four-wave mixing in gas-filled hollow-core photonic crystal fiber," Opt. Lett. **44**(22), 5509–5512 (2019).
26. R. Forbes, P. Hockett, Q. Leterrier, *et al.*, "Efficient (~10 % ) generation of vacuum ultraviolet femtosecond pulses via four-wave mixing in hollow-core fibers," Opt. Lett. **49**(11), 3178–3181 (2024).
27. I. Brener, P. P. Mitra, D. D. Lee, *et al.*, "High-resolution zero-dispersion wavelength mapping in single-mode fiber," Opt. Lett. **23**(19), 1520–1522 (1998).
28. R. J. A. Francis-Jones and P. J. Mosley, "Characterisation of longitudinal variation in photonic crystal fibre," Opt. Express **24**(22), 24836–24845 (2016).
29. J. M. Dudley, G. Genty, and S. Coen, "Supercontinuum generation in photonic crystal fiber," Rev. Mod. Phys. **78**(4), 1135–1184 (2006).
30. S. A. Mousavi, H. C. H. Mulvad, N. V. Wheeler, *et al.*, "Nonlinear dynamic of picosecond pulse propagation in atmospheric air-filled hollow core fibers," Opt. Express **26**(7), 8866–8882 (2018).
31. D. Marcuse, C. Manyuk, and P. Wai, "Application of the Manakov-PMD equation to studies of signal propagation in optical fibers with randomly varying birefringence," J. Lightwave Technol. **15**(9), 1735–1746 (1997).
32. Á. Börzsönyi, Z. Heiner, A. Kovács, *et al.*, "Measurement of pressure dependent nonlinear refractive index of inert gases," Opt. Express **18**(25), 25847–25854 (2010).
33. E. T. J. Nibbering, G. Grillon, M. A. Franco, *et al.*, "Determination of the inertial contribution to the nonlinear refractive index of air, N_2, and O_2 by use of unfocused high-intensity femtosecond laser pulses," J. Opt. Soc. Am. B **14**(3), 650–660 (1997).
34. V. Loriot, E. Hertz, O. Faucher, *et al.*, "Measurement of high order Kerr refractive index of major air components," Opt. Express **17**(16), 13429–13434 (2009).
35. R. Schiek, "Nonlinear refractive index in silica glass," Opt. Mater. Express **13**(6), 1727–1740 (2023).
36. M. E. Marhic, *Fiber optical parametric amplifiers, oscillators and related devices* (Cambridge University, 2008), 1st ed.
37. T. W. Kelly, P. Horak, I. A. Davidson, *et al.*, "Gas-induced differential refractive index enhanced guidance in hollow-core optical fibers," Optica **8**(6), 916–920 (2021).
38. G. T. Jasion, J. R. Hayes, N. V. Wheeler, *et al.*, "Fabrication of tubular anti-resonant hollow core fibers: modelling, draw dynamics and process optimization," Opt. Express **27**(15), 20567–20582 (2019).
39. E. Elistratova, T. W. Kelly, I. A. Davidson, *et al.*, "Distributed Measurement of Hollow-Core Fibre Gas Filling and Venting via Optical Time-Domain Reflectometry," in *2023 Conference on Lasers and Electro-Optics Europe & European Quantum Electronics Conference (CLEO/Europe-EQEC)*, (IEEE, Munich, Germany, 2023). Paper CE-2.4.
40. X. Wei, E. Numkam Fokoua, F. Poletti, *et al.*, "Extraction of Attenuation and Backscattering Coefficient along Hollow-Core Fiber Length Using Two-Way Optical Time Domain Backscattering," ACS Photonics **11**, 4076–4082 (2024).
41. Mitchell Gerrard, Peter Horak, and Radan Slavik, "Dataset supporting 'Distributed Measurement of Gas Pressure in the Core of Hollow-Core Optical Fibres using Nonlinear Optics'," University of Southampton (2025).